ACS APPLIED MATERIALS & INTERFACES

www.acsami.org

Research Article

Electro- and Photoinduced Interfacial Charge Transfers in Nanocrystalline Mesoporous TiO_2 and TiO_2/Iron Porphyrin Sensitized Films under CO_2 Reduction Catalysis

Beatriu Domingo-Tafalla, Tamal Chatterjee,* Federico Franco, Javier Perez Hernandez, Eugenia Martinez-Ferrero, Pablo Ballester,* and Emilio Palomares*

Cite This: *ACS Appl. Mater. Interfaces* 2023, 15, 14304−14315

Read Online

ACCESS | Metrics & More | Article Recommendations | Supporting Information

ABSTRACT: Electro- and photochemical CO_2 reduction (CO_2R) is the quintessence of modern-day sustainable research. We report our studies on the electro- and photoinduced interfacial charge transfer occurring in a nanocrystalline mesoporous **TiO_2** film and two **TiO_2**/iron porphyrin hybrid films (*meso*-aryl- and *β*-pyrrole-substituted porphyrins, respectively) under CO_2R conditions. We used transient absorption spectroscopy (TAS) to demonstrate that, under 355 nm laser excitation and an applied voltage bias (0 to −0.8 V vs Ag/AgCl), the **TiO_2** film exhibited a diminution in the transient absorption (at −0.5 V by 35%), as well as a reduction of the lifetime of the photogenerated electrons (at −0.5 V by 50%) when the experiments were conducted under a CO_2 atmosphere changing from inert N_2. The **TiO_2**/iron porphyrin films showed faster charge recombination kinetics, featuring 100-fold faster transient signal decays than that of the **TiO_2** film. The electro-, photo-, and photoelectrochemical CO_2R performance of the **TiO_2** and **TiO_2**/iron porphyrin films are evaluated within the bias range of −0.5 to −1.8 V vs Ag/AgCl. The bare **TiO_2** film produced CO and CH_4 as well as H_2, depending on the applied voltage bias. In contrast, the **TiO_2**/iron porphyrin films showed the exclusive formation of CO (100% selectivity) under identical conditions. During the CO_2R, a gain in the overpotential values is obtained under light irradiation conditions. This finding was indicative of a direct transfer of the photogenerated electrons from the film to absorbed CO_2 molecules and an observed decrease in the decay of the TAS signals. In the **TiO_2**/iron porphyrin films, we identified the interfacial charge recombination processes between the oxidized iron porphyrin and the electrons of the TiO_2 conduction band. These competitive processes are considered to be responsible for the diminution of direct charge transfer between the film and the adsorbed CO_2 molecules, explaining the moderate performances of the hybrid films for the CO_2R.

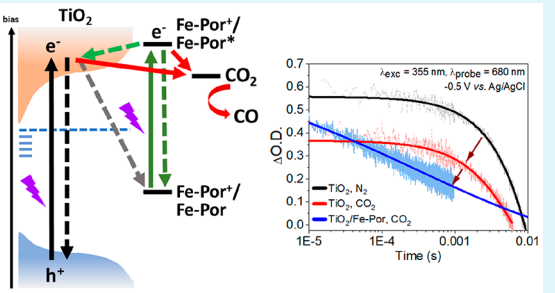

KEYWORDS: *electro- and photochemical CO_2 reduction, mesoporous TiO_2 film, mesoporous TiO_2/iron porphyrin hybrid films, interfacial charge transfers, laser transient absorption spectroscopy*

1. INTRODUCTION

In the coming decades, enabling an infrastructure to produce commodity chemicals and fuels using renewable energy to fulfill global demand is a necessary challenge. Worldwide active research is going on to make such a novel industry in hard reality.[1,2] Solar-driven water splitting and CO_2 reduction (CO_2R) are longstanding routes for the sustainable production of carbon-based fuels and feedstocks, as they can be easily utilized in existing fossil-fuel-assisted energy infrastructure.[3−5] The ultimate inspiration to perform artificial water splitting and CO_2 reduction started with emulating natural photosynthesis. Nature performs the machinery in several concerted redox-favored processes, from light-triggered single-electron-transfer events to multielectron catalysis processes. Similarly, the artificial version of photosynthesis is envisaged by designing a hybrid assembly that integrates light absorption, electron transfer, and catalysis concurrently.[6,7] For the CO_2R, such an assembly can be incorporated as a photocathode, in which nanocrystalline semiconductor materials can be used to generate and store multiple charges for a considerable time with the accessible band gap across the solar spectrum and a molecular catalyst counterpart that can perform the multiredox electro- or photoelectrochemical CO_2 reduction with optimum activity and product selectivity.[8] The quest for developing CO_2R photocathodes has been well documented in recent reviews covering the various combination of light-absorbing semiconductors (p-type Si, GaP, GaAs, n-type TiO_2, ZnO,

Received: December 13, 2022
Accepted: February 23, 2023
Published: March 7, 2023

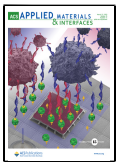

NiO, Cu_2O, etc.) and transition-metal-based molecular catalysts such as Re(vinyl-bpy)$(CO)_3Cl$, Ru(bpy-R_2)$(CO)_2Cl_2$ (R = PO_3H_2, COOH), Ni(cyclam)$^{2+}$, Re(bpy)$(CO)_3Cl$, Fe-porphyrin, Co(II) bis(terpyridine), etc.[8−10] For hybrid electrode fabrication, the desired covalent immobilization of the molecular catalyst over the semiconductor surface is obtained either by electropolymerization or via phosphonic, carboxylic, and hydroxamate anchoring groups.[8] Different types of hybrid systems showed photocurrents in the range of 100−150 mA cm^{-2} to 0.5−3 mA cm^{-2} with moderate stability, having CO as the main CO_2R product along with CH_3COOH, $HCOO^-$, and CH_3OH as minor products, although the formation of $C_{\geq 2}$ reduced products remains elusive.[8,9] Many reports have explored different types of catalyst immobilizations, dissimilar anchoring methods, CO_2R product selectivity, and the overall stability of the photocathodes. However, the number of reports focusing on investigating the interfacial charge-transfer events occurring in the hybrid electrodes is low. This point is especially relevant due to the fact that poor charge accumulation and fast recombination of charges have a major impact on the multiredox reactions occurring at the molecular catalysts and thereby limit the overall photocathode CO_2R efficiency.[11] CO_2R involves multielectron and multiproton transfer processes; therefore, by tuning the band gap and the conduction band energy of the semiconductor pertinent to the energy levels of the molecular catalysts provide scope to improve the interfacial electron transfers from the semiconductor to the molecular catalyst. The optimization of the energy levels of the photocathode components enhances the photoelectrochemical CO_2R efficiency and feasibility of seldom $C_{\geq 2}$ product formation.[12] Hence, the study of the interfacial charge transfer kinetics of such hybrid photocathodes has become of special interest. Durrant et al. have conducted important studies in this area. For instance, they explored the correlation between the photoelectrochemical hydrogen evolution and CO_2R activity with the lifetime of the charge-separated state formed in the hybrid systems made up of TiO_2−Co(II) terpyridine/cobaloxamine complexes via phosphonic acid linkages.[13−15] Under light irradiation, charge accumulation, Co(II)/Co(I) redox shuttling, and transfer kinetics of the TiO_2 excited electron to the Co(II) catalysts showed a dependence on light intensity, applied external bias, catalyst loading, and the length of the linkers spanning the cobalt ion from the TiO_2 surface.

For our current study, we constructed a model photocathode system made of mesoporous TiO_2 and iron porphyrins as a molecular catalyst. We aimed at studying the interfacial charge transfer processes taking place during the CO_2R reaction. The choice of TiO_2 was guided by its advantageous properties, including transparency, stability, low cost, and its wide use in studies of dye-sensitized solar cells (DSSCs).[10,16,17] For the CO_2R, bare nanocrystalline mesoporous TiO_2 is known to undergo multielectron-transfer processes to adsorb CO_2, resulting in the formation of CH_3OH and CO in acetonitrile. These electron-transfer processes were further examined by using spectroelectrochemical (ATR-IR and UV−vis) methods.[18,19] On the other hand, iron porphyrin families with modified *meso*-aryl groups are well-known catalysts for the electrochemical transformation of CO_2 to CO with high Faradaic efficiency and overpotential values between 220 and 800 mV, depending on the solvent systems.[20] Furthermore, the catalytic activity of iron porphyrins was also explored in flow cell electrolyzers. In this case, the iron porphyrins were employed as catalytic films obtained from their heterogenization onto nanocarbon support materials.[21] Heterogenization of iron porphyrins on semiconductor supports has been previously reported; Naruta et al. studied CO_2 to CO conversion with an Fe *meso*-arylporphyrin immobilized on FTO-SnO_2 and FTO-TiO_2 surfaces by using phosphonic acid as an anchor group.[22] Moore et al. studied the hydrogen evolution reaction (HER) after covalent grafting of Co and Fe *meso*-arylporphyrins on a GaP semiconductor.[23] More recently, the Aukauloo group investigated charge accumulation during the photocatalytic CO_2R mediated by an Fe porphyrin, $[Ru(bpy)_3]^{2+}$ as photosensitizer, and DMF as solvent. These studies suggested the possibility of an alternate mechanism for the CO_2R involving a Fe(I) intermediate instead of the Fe(0) counterpart invoked in the classical pathway.[24,25] Meyer et al. reported a non-Nernstian type multielectron transfer using mesoporous TiO_2-Co(II) *meso*-aryl porphyrin heterogeneous films. They performed nano- to microsecond transient absorption spectroscopy experiments upon excitation of the Co porphyrin at 532 nm. Nevertheless, they did not undertake any study of the catalysis.[26] To the best of our knowledge, studies of the intriguing interfacial charge transfer and charge recombination processes taking place on mesoporous **TiO_2** and **TiO_2**/iron porphyrin films for the CO_2R under operando conditions have not been reported and we decided to focus on them in this work.

Herein, we report two model hybrid material-based catalysts for the CO_2R. The catalysts consist of a mesoporous nanocrystalline anatase polymorph TiO_2 functionalized with two different iron porphyrin-based catalysts. Specifically, from the iron porphyrin family, we choose (1) the commercially available hemin (**Hem**), a protoporphyrin IX ligand containing Fe(III) as a central metal atom having an axial chloride ligand, and (2) a A_3B type Fe(III) *meso*-tetraphenylporphyrin (**Fe-Por**) bearing three pentyl chains and one carboxylic acid group in the *para* positions of its *meso*-phenyl groups (Chart 1). We

Chart 1. (Left) Cartoon Representation of the Glass-FTO-TiO_2 Surface Used for the Covalent Anchoring of the Porphyrin Derivatives and (Right) Molecular Structures of the Iron Porphyrins (Hem and Fe-Por) Employed in the Preparation of the Porphyrin Hybrid Assemblies

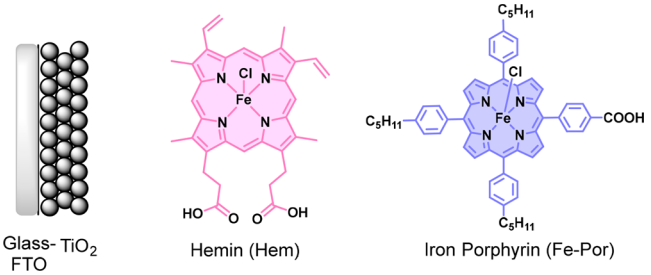

report the synthesis, characterization, interfacial charge transfer kinetics, and catalytic performances in the CO_2R reaction of these two **TiO_2**/iron porphyrin hybrid assemblies. We also compare their performances with that of a mesoporous **TiO_2** film used as a reference.

2. RESULTS AND DISCUSSION

2.1. Preparation and Characterization of the TiO_2/Iron Porphyrin (Hem and Fe-Por) Films. The free base 5-(4-carboxyphenyl)-10,15,20-tris(4-pentylphenyl)porphyrin has

https://doi.org/10.1021/acsami.2c22458
ACS Appl. Mater. Interfaces 2023, 15, 14304−14315

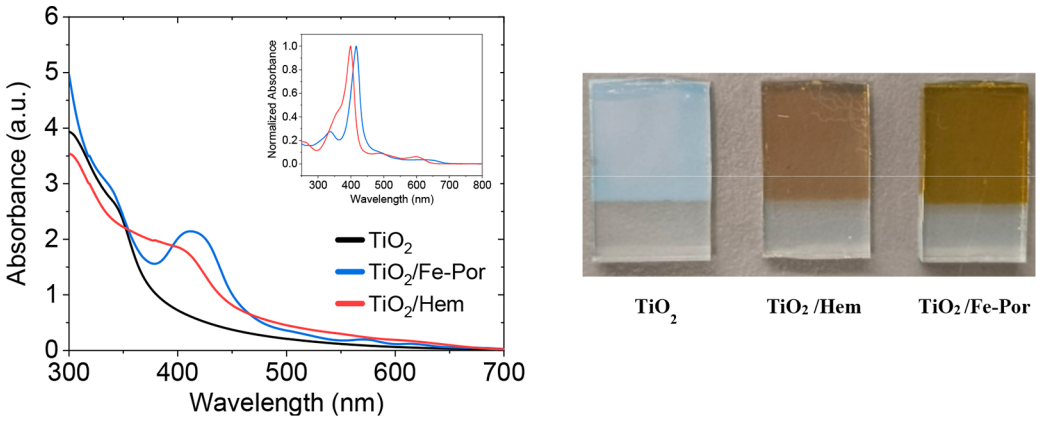

Figure 1. (left) UV−visible spectra of Hemin (**Hem**) and Fe-porphyrin (**Fe-Por**) on a transparent 5 μm thick mesoporous TiO_2 film measured in air with the normalized absorption spectra of only **Hem** and **Fe-Por** porphyrins in CH_3OH solution being shown in the inset. (right) Visual appearance of the **TiO_2**, **TiO_2/Hem**, and **TiO_2/Fe-Por** films on FTO glass.

been previously explored as sensitizer in TiO_2 solar cells,[27] in which the role of the *para*-pentyl chains in the *meso*-phenyl substituents was proved effective to deter porphyrin aggregation on the TiO_2 layer. The Fe metalation of the porphyrin core yielded **Fe-Por** (the detailed synthesis process is described in the Supporting Information), and its absorption characteristics and ^{1}H NMR shifts are in good agreement with those of similar iron porphyrins reported in the literature.[28−30] We prepared separate solutions of **Hem** and **Fe-Por** in methanol by prolonged sonication of the initial suspensions. Subsequently, the Fe porphyrin derivatives were readily immobilized on the mesoporous TiO_2 surface using a dip-coating methodology. Most likely, the porphyrins were covalently anchored on the TiO_2 surface via the typical bidentate chelating mode of their carboxylic groups.[31] The resulting films were stable at room temperature and kept in the dark until use (Figure 1).

The absorption maxima of **Hem** and **Fe-Por** in MeOH solution were observed at λ = 400 and λ = 416 nm, respectively, with broad Q-bands in the region of λ = 500−650 nm (Figure 1, inset). However, upon anchoring the porphyrins to the TiO_2 surface, their absorption spectra experienced significant broadening, which can be attributed to the light-scattering effect of the mesoporous TiO_2.[32,33] The **TiO_2/Hem** and **TiO_2/Fe-Por** hybrid assemblies showed broad Soret bands with maxima at λ = 404 and λ = 414 nm, respectively, and weakly absorbing Q-bands (Figure 1). Adsorption kinetics studies showed that the adsorption of both iron porphyrins on the TiO_2 surface reached a plateau within 20 min (Figure S4 in the Supporting Information). Approximately, this should correspond to a monolayer of covalently anchored porphyrins on the TiO_2 surface. Thus, we conclude that despite the **Hem** and **Fe-Por** having structural differences (*meso*-aryl and β-substituents) and possessing different numbers of anchoring −COOH groups, they experience similar adsorption kinetics onto the TiO_2 surface. The average loading of the iron porphyrins on the TiO_2 was estimated from the UV−visible measurements of solutions obtained after leaching treatments of the **TiO_2/Fe-Por** and **TiO_2/Hem** under a high reductive and mild oxidative potential (cycles between −1.8 and 0.8 V vs Ag/AgCl). This result also evidenced the low stability of the linkages between the porphyrin carboxylic group and the TiO_2 surface under the above electrochemical conditions. We estimated that the average loading of the iron porphyrins on the **TiO_2/Hem** and **TiO_2/Fe-Por** films are 11 ± 3 and 22 ± 3 nmol cm^{-2}, respectively (Figure S4). The variation in loading arises from the different structures of the Fe porphyrins, but both values are comparable with those previously reported for cobalt porphyrin loadings on mesoporous TiO_2.[26] However, they are smaller than those of cobalt complexes bearing phosphonic acid anchors.[14] Attenuated total reflection infrared (ATR-IR) spectroscopy was also used for the characterization of **TiO_2/Hem** and **TiO_2/Fe-Por** hybrid assemblies (spectra are presented in Figures S5 and S6). In **Fe-Por**, the Fe−N bond stretching frequency was centered at ∼1000 cm^{-1}, those of the C−H bonds of benzene and pyrrole appeared at ∼2923−2852 cm^{-1}, the C═C stretching mode at ∼1494−1687 cm^{-1}, and that of the C═N at ∼1333 cm^{-1}. Also, bands at 1733 and 1272 cm^{-1} are assigned to the characteristic C═O and C−O stretching of the carboxylic acid group, respectively. The values follow the same trend as reported for other iron(III) chloride porphyrin complexes.[34,35] The broad peaks at ∼3400 and ∼1650 cm^{-1} for the FTO-TiO_2 film correspond to the stretching vibration of hydroxyl functional groups and bending vibration of free water, respectively.[36] The spectrum of **TiO_2/Fe-Por** showed the near disappearance of C═O and C−O stretching modes of the free carboxylic acid group, confirming the anchoring of **Fe-Por** on the TiO_2 surface. However, in the **TiO_2/Fe-Por** spectrum, broadening of the **Fe-Por** signals is attributed to the presence of a nanomolar amount of porphyrin loading compared to a high excess of TiO_2 molecules (3.91 μmol cm^{-2} of TiO_2). The IR spectrum of **TiO_2/Hem** exhibited similar characteristics feature (Figure S6). XPS analysis was further carried out with the **TiO_2**, **TiO_2/Hem**, and **TiO_2/Fe-Por** films (Figures S7 and S8). In **TiO_2**, the Ti $2p_{1/2}$ and Ti $2p_{3/2}$ peaks appeared at 464.4 and 458.7 eV, respectively, which matches the literature report.[37] There is no marked shift and no shape change in the Ti $2p_{1/2}$ and Ti $2p_{3/2}$ signals when comparing bare TiO_2 to TiO_2/iron porphyrins films, which confirms that there is no change in the coordination and electronic environment of Ti in TiO_2 after the porphyrin loading. Furthermore, Figure S8 reveals the Fe 2p signals at ∼709−711 eV (Fe $2p_{3/2}$) and ∼723 eV (Fe $2p_{1/2}$) in **TiO_2/Hem** and **TiO_2/Fe-Por** films, respectively, which is in accordance with the +III oxidation state of iron.[38] Thus, an XPS analysis confirms the presence and anchoring of the iron(III) porphyrin structures in the hybrid catalyst films.

https://doi.org/10.1021/acsami.2c22458
ACS Appl. Mater. Interfaces 2023, 15, 14304−14315

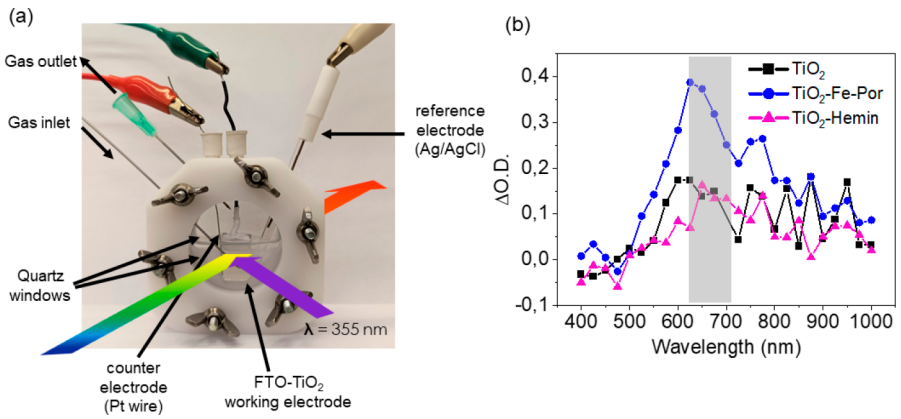

Figure 2. (a) Picture of the Teflon L-TAS cell setup with double quartz windows, equipped for measurements under a controlled atmosphere and applied external bias. (b) Survey L-TAS spectra of **TiO_2**, **TiO_2/Hem**, and **TiO_2/Fe-Por** films measured in acetonitrile solution containing 0.1 M $TBAPF_6$ after λ = 355 nm excitation under an N_2 atmosphere. The probe wavelength was fixed at λ = 680 nm.

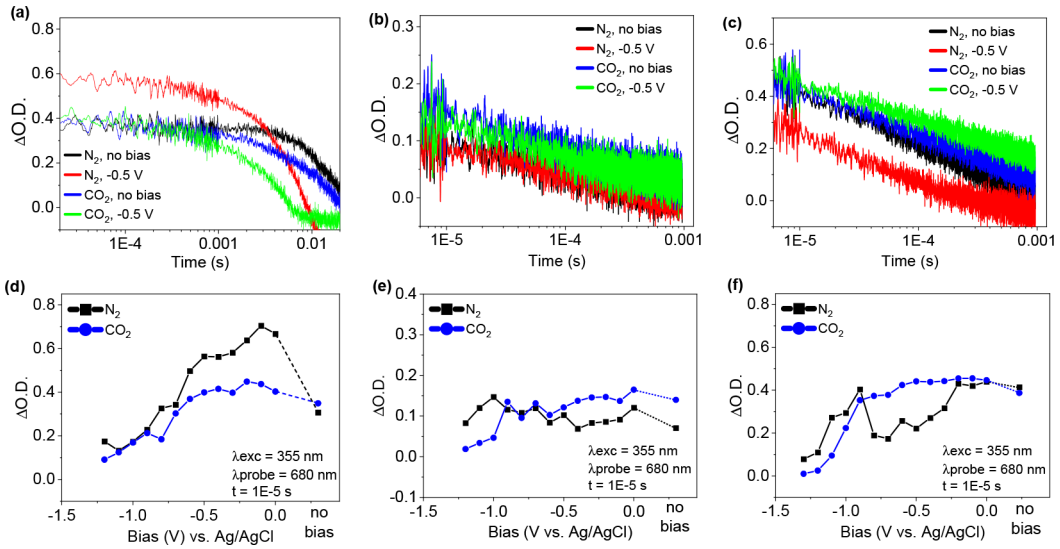

Figure 3. TAS spectra of (a) **TiO_2**, (b) **TiO_2/Hem**, and (c) **TiO_2/Fe-Por** recorded in the presence of acetonitrile containing 0.1 M $TBAPF_6$ after excitation at λ = 355 nm and under N_2 and CO_2 atmospheres using applied bias (−0.5 V vs Ag/AgCl) conditions. Only the L-TAS of **TiO_2** was measured in the presence of 0.01 M TEOA as a hole scavenger. (d−f) Comparison of the transient absorption for **TiO_2**, **TiO_2/Hem**, and **TiO_2/Fe-Por**, respectively, acquired under N_2 and CO_2 atmospheres. The TAS spectra were recorded by applying a bias of 0 to −1.2 V vs Ag/AgCl. The transient absorption values were taken at the time 1×10^{-5} s. The probe wavelength was fixed at λ = 680 nm.

2.2. Interfacial Charge Transfer Kinetics. Laser transient absorption spectroscopy (L-TAS) was employed to investigate the charge transfer and recombination kinetics between the components of the **TiO_2**/iron porphyrin hybrid assemblies by monitoring the charge carrier lifetimes (Figure 2a). For our current study, we focused on micro- to millisecond charge carrier lifetimes of TiO_2 and their corresponding values pertinent to the CO_2R reaction. Transient decays of the anatase TiO_2 photoelectron in an acetonitrile-$TBAPF_6$ (supporting electrolyte) solution under an N_2/CO_2 atmosphere were measured following a band gap excitation at λ = 355 nm. After laser excitation at λ = 355 nm in the dark of the **TiO_2** film, the survey spectrum (black trace in Figure 2b) showed transient absorption throughout the λ = 600−900 nm range, where the electrons in the conduction band of TiO_2 absorb. We chose to study and compare all our results with the λ = 680 nm transient absorption signals and obscure the λ = 690−710 nm region signals to avoid any interference in the signals arising from the second harmonics of the excitation wavelength (λ_{exc} = 355 nm; λ_{har} = 710 nm).

Previously, it has been also shown that the use of a chemical scavenger during the L-TAS measurement can specifically quench either the electrons ($AgNO_3$) or the holes (methanol or amine) depending on the choice.[14,39] In the present case, we were particularly interested in the photogenerated electrons and their recombination kinetics during the CO_2R reaction. Hence, we used a sacrificial hole scavenger (triethanolamine, TEOA) to quench the TiO_2 photogenerated holes during the measurement. The use of TEOA as a hole scavenger increased the lifetime of the photoexcited electrons and induced an increment in the amplitude of the transient absorption signal (Figure S9a). Thus, in the presence of 0.01 M TEOA (black trace in Figure 3a), we corroborated that the photoexcited electrons in **TiO_2** exhibit decay kinetics on the millisecond time scale following typical stretched exponential kinetics.[40−42]

Next, to mimic a typical photoelectrochemical CO_2 reduction experiment, we purged CO_2 into the electrolyte and/or we applied a bias varying from 0 to −1.3 V vs Ag/AgCl to the **TiO_2** film. In doing so, we fixed the Fermi level at the TiO_2 electrode. Ideally, this bias range is less than the TiO_2

https://doi.org/10.1021/acsami.2c22458
ACS Appl. Mater. Interfaces 2023, 15, 14304−14315

(a)

FTO-TiO_2			
Conditions		$\Delta O.D._{max}$	$t_{50\%}$ (s)
N_2	no bias	0.36	0.012
	-0.2 V	0.62	0.0036
	-0.5 V	0.58	0.0041
CO_2	no bias	0.36	0.0083
	-0.2 V	0.4	0.0018
	-0.5 V	0.4	0.0021

(b)

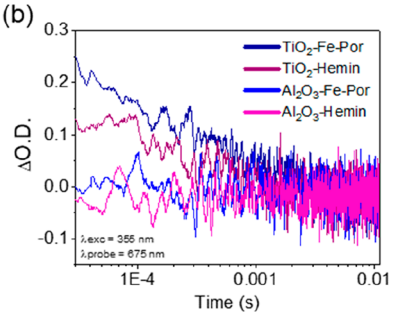

Figure 4. (a) Table of the $t_{50\%}$ values obtained with the TAS measurements on TiO_2 films. (b) Comparison of TAS spectra of **Al_2O_3/Hem** and **Al_2O_3/Fe-Por** with those of **TiO_2/Hem** and **TiO_2/Fe-Por** in acetonitrile containing 0.1 M $TBAPF_6$ after excitation at λ = 355 nm under an N_2 atmosphere and without an applied bias voltage. The probe wavelength was fixed at λ = 675 nm.

conduction band potential, so that we restrict the continuum filling of the valence band to the conduction band level of TiO_2. However, we observed differences in the decay kinetics of the photogenerated TiO_2 electron when CO_2 was purged in the electrolyte even in the absence of applied potential. In fact, under a CO_2 atmosphere, the transient signal intensity remains at the same ΔOD initial value but its lifetime is shortened in comparison to an N_2 atmosphere (blue trace in Figure 3a). The corresponding "$t_{50\%}$" values (time taken to reach half of the transient absorption amplitude values, ΔOD) and maximum ΔOD at λ = 680 nm are compared in Figure 4a; $t_{50\%}$ decreases from 12 ms under an N_2 atmosphere to 8 ms under a CO_2 atmosphere. Afterward, we chose in particular a bias of −0.5 V (vs Ag/AgCl) to compare the transient decay with the nonbiased case under N_2 and CO_2 atmospheres (red and green traces in Figure 3a). The overlay of all the transient decays recorded in the range of 0 to −1.3 V vs Ag/AgCl applied bias under N_2 and CO_2 atmospheres for the **TiO_2** film is shown in Figure S10a,b. Under N_2 and −0.5 V applied bias (vs Ag/AgCl) the transient signal intensity of the **TiO_2** film increases while the $t_{50\%}$ value decreases to 4 ms in comparison to a no-bias experiment (red trace in Figure 3a). Most likely, this is due to the fact that the tail states below the TiO_2 conduction, which are likely involved in the trapping of the photogenerated electrons, are filled up electrochemically.

Under CO_2, an application of the external bias produces a marked difference from the transient decay for the N_2 atmospheres. With CO_2, the maximum transient absorption decreases by 0.2 ΔOD, and the lifetime of photogenerated electrons features a reduced $t_{50\%}$ value of 2 ms (green trace in Figure 3a). When bias is applied, in the 0 to −1 V (vs Ag/AgCl) region, the maximum absorption values, measured at time 1×10^{-5} s, also show noticeable differences between N_2 and CO_2 atmospheres (Figure 3d). The absorption value under a CO_2 atmosphere always remains lower than that of the experiment under N_2. For both cases, after applying −1 V vs Ag/AgCl, the transient signal starts to disappear due to electrochemical filling up of the conduction band of TiO_2 with electrons.

We conducted the same measurements for **TiO_2/Hem** and **TiO_2/Fe-Por** films, and we observed some differences in the transient absorption signals compared to the bare **TiO_2** film (Figure 3b,c). First, the use of TEOA in the case of the **TiO_2/Fe-Por** and **TiO_2/Hem** films did not have any improvement effects in the transient absorption or in the decay kinetics (Figure S9b,c). This observation is remarkably different from that observed previously for the bare **TiO_2**, suggesting that TEOA does not stabilize the oxidized porphyrin catalyst. For this reason, we skipped the use of TEOA in the TAS measurements of **TiO_2/Hem** and **TiO_2/Fe-Por** films. Second, the presence of **Fe-Por** on the TiO_2 caused an increase of the transient signal in the region of λ = 550−800 nm, with a maximum at λ = 650 nm (blue trace in Figure 2b). In the case of **Hem** a related but less defined transient absorption spectrum was observed (pink trace in Figure 2b). The recorded signal in both spectra correspond to the oxidized porphyrin catalysts as a result of the photoinduced electron injection to the TiO_2 conduction band. Third, under identical conditions, we observed that for the **TiO_2/Hem** and **TiO_2/Fe-Por** films their transient decays are 100 times faster than that of the bare **TiO_2** film. The transient signal of the porphyrin-functionalized films disappeared by 1 ms (Figure 3b,c). Last but not least, the initial steady state (time scale faster than 1 μs) is not clearly recordable within our time resolution range. This is particularly important for **TiO_2/Hem**, with ΔOD as low as 0.1 ΔOD. This limitation does not allow us to determine accurate initial transient absorption and $t_{50\%}$ values for the **TiO_2/Fe-Por** and **TiO_2/Hem** hybrid systems. Moreover, these findings indicate the existence of faster charge recombination processes in the hybrid systems compared to the bare **TiO_2** film.[26,43,44]

By looking in more detail at the effect of the presence of CO_2 and the application of bias to the **TiO_2/Hem** and **TiO_2/Fe-Por** films, we observed a different behavior of the hybrid films in comparison to bare **TiO_2**. Under an N_2 atmosphere, the application of −0.5 V caused a reduction in the transient signal (red trace in Figure 3b,c). The reduction of the intensity was more significant for the **TiO_2/Fe-Por** film than for the **TiO_2/Hem** counterpart. The presence of CO_2 does not pronouncedly affect the L-TAS signal in the nonbiased case but, interestingly, it prevents the decrease in the transient signal when a −0.5 V bias is applied (blue and green traces in Figure 3b,c). Overlays of the transient absorption decays recorded over the range of 0 to −1.3 V vs Ag/AgCl applied bias under N_2 and CO_2 atmospheres are shown in Figure S10c−f. In the 0 to −1 V vs Ag/AgCl range, the maximum transient absorption values obtained at time 1×10^{-5} s showed that **TiO_2/Fe-Por** and **TiO_2/Hem** follow similar trends (Figure 3e,f) with always smaller ΔOD amplitude transient signals for **TiO_2/Hem**. For the **TiO_2/Fe-Por** film under an N_2 atmosphere, the maximum of the transient signal decreases with negative bias until −0.8 V vs Ag/AgCl is applied. In contrast, under a CO_2 atmosphere, the application of a negative bias does not have a significant effect on the maximum of the transient signal until a bias of −1 V vs Ag/AgCl is applied. Under N_2 and CO_2 atmospheres, the

https://doi.org/10.1021/acsami.2c22458
ACS Appl. Mater. Interfaces 2023, 15, 14304−14315

Table 1. CO_2R Performances of the TiO_2 Film and TiO_2/Hem and TiO_2/Fe-Por Hybrid Films under Electro-, Photo-, and Photoelectrochemical Conditions[a]

		without light irradiation			with 365 nm LED irradiation		
electrode	potential (vs Ag/AgCl)	product	production rate (nmol h^{-1} cm^{-2})	selectivity (%)[b]	product	production rate (nmol h^{-1} cm^{-2})	selectivity (%)[b]
FTO-TiO_2	no bias				CO	22 ± 2	100
					CH_4	traces	
	−0.5				CO	19 ± 3	56
					CH_4	15 ± 2	44
	−1.25				CO	51 ± 10	51
					CH_4	48 ± 10	49
	−1.5	H_2	140	100	H_2	160 ± 9	70
					CO	67 ± 2	30
	−1.8	H_2	496 ± 118	85			
		CO	90 ± 51	15			
FTO-TiO_2/Hem	no bias				CO	17 ± 2	100
	−0.5				CO	19 ± 8	100
	−1.25				CO	29 ± 3	100
	−1.5	CO	280 ± 60	100	CO	211 ± 1	100
	−1.8			leaching of porphyrin			
FTO-TiO_2/Fe-Por	no bias				CO	25	100
	−0.5				CO	40 ± 10	100
	−1			leaching of porphyrin			

[a]Measurements were done in a single-compartment cell using Pt wire as the counter electrode, Ag/AgCl as the reference electrode, and acetonitrile solution containing 0.1 M $TBAPF_6$ as the supporting electrolyte. [b]Selectivity = mol of one product/mol of total product formed.

application of potentials more negative than −1 V induced the disappearance of the transient signals. This is due to the existence of very fast charge recombination kinetics between the electrons at the TiO_2 conduction band and the oxidized catalyst.

As a control system, we prepared an iron porphyrin supported on Al_2O_3 nanocrystalline mesoporous films. We chose Al_2O_3 since the energy values of the conduction band (∼−1.5 eV vs vacuum) of this metal oxide (high compared to TiO_2 ∼−4.5 eV vs vacuum) prevents efficient photoinduced electron transfer from the porphyrin's excited state upon λ = 355 nm excitation.[45] Figure 4b presents a comparison of the TAS signals of the hybrid assemblies with immobilized iron porphyrin on TiO_2 and of Al_2O_3 analogues. As expected, no transient absorption signals are observed in case of **Al_2O_3/Hem** and **Al_2O_3/Fe-Por** hybrid assemblies. Furthermore, we also performed L-TAS by exciting the TiO_2/iron porphyrin assemblies at the Soret and first Q-band of the Fe porphyrin (excited with λ = 420 nm and λ = 500 nm for **TiO_2/Hem** or λ = 530 nm for **TiO_2/Fe-Por**, laser). We monitored the transient absorption signals associated with the excited porphyrins. Notably, we did not observe any transient signals using **TiO_2/Hem** at the millisecond time scale (Figure S11b) at both excitation wavelengths. Conversely, for the **TiO_2/Fe-Por** hybrid, the excitation at 420 and 530 nm produced a weak transient signal at 650 nm (Figure S11a) in the millisecond time scale. The nanocrystalline mesoporous TiO_2 film does not have a significant absorption at 420 and 530 nm. Thus, the transient decay must be due to the photoinjection of electrons in the TiO_2 conduction band from the photoexcited iron porphyrin. This result is in good agreement with our previous measurements depicted in Figure 2b for the **TiO_2/Fe-Por** film. In short, the results of the control studies support that, for the **TiO_2/Hem** and **TiO_2/Fe-Por** sensitized films, the transient decays correspond to the photoinduced charge recombination kinetics between the electrons at the TiO_2 conduction band and the oxidized porphyrins.

We became interested in studying the electron transfer kinetics of these hybrid systems for the CO_2R under operando conditions. Thereby, we studied the fate and efficiency of the hybrid systems during the CO_2R using similar L-TAS conditions.

2.3. CO_2 Reduction Studies using TiO_2, TiO_2/Hem, and TiO_2/Fe-Por Films. To understand the CO_2R performances using the **TiO_2/Hem** and **TiO_2/Fe-Por** films, we investigated the process in a one-compartment glass cell under both electro- and photoelectrochemical conditions. The cyclic voltammograms (CV) of **Hem** and **Fe-Por** in homogeneous DMF solution showed three typical iron-center-based reduction peaks ($Fe^{III/II}$, $Fe^{II/I}$, $Fe^{I/0}$) (**Hem**, −0.35, −1.21, −1.81 V; **Fe-Por**, −0.24, −1.06, −1.67 vs Ag/AgCl). The CV experiments were carried out under an argon atmosphere and using ferrocene as an internal standard (Figure S12a). Further, in the presence of CO_2, we observe a catalytic current response at the $Fe^{I/0}$ wave in both cases (Figure S12b,c). In a DMF solution, the controlled-potential electrolysis (at −1.6 V vs Ag/AgCl for **Fe-Por** or −1.7 V vs Ag/AgCl for **Hem**) produced exclusively CO as the CO_2R product for both iron porphyrins. The CV of the bare **TiO_2** film in acetonitrile solution under an argon atmosphere exhibited the appearance of a signal at −1.3 V vs Ag/AgCl. This value matched well with the reported reduction of Ti^{4+} to Ti^{3+} at the TiO_2 surface (Figure S13a).[18] In the presence of CO_2, an increase in the reduction current is noticed to have an onset at the same −1.3 V potential. It is important to note that the −1.3 V vs Ag/AgCl potential is greater than the TiO_2 conduction band edge and at this potential accumulation of electron-rich Ti^{3+} species at the surface of the film is initiated. These species are key for the

https://doi.org/10.1021/acsami.2c22458
ACS Appl. Mater. Interfaces 2023, 15, 14304−14315

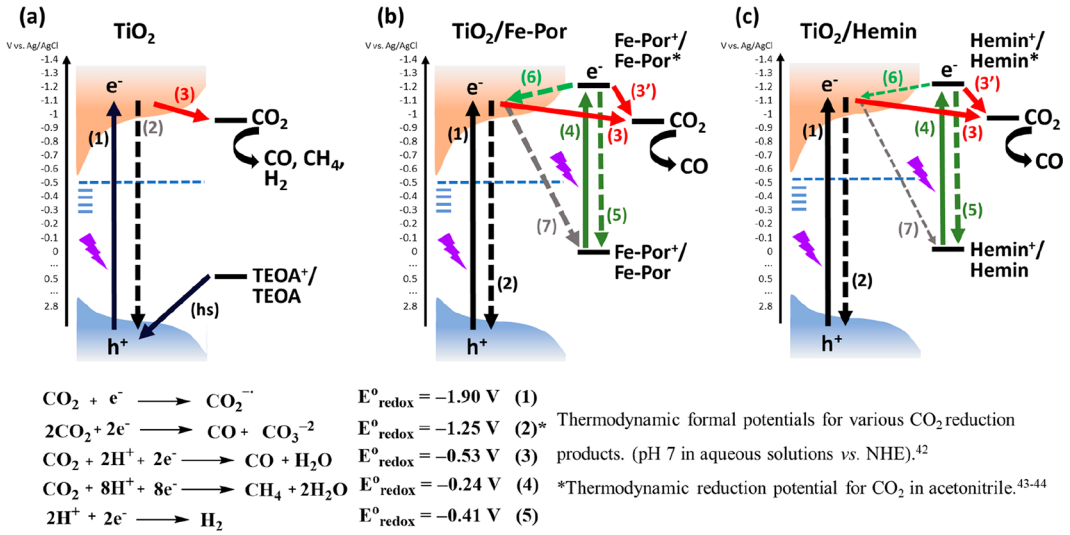

Figure 5. Suggested pathways for the different electron transfer processes occurring in (a) **TiO_2**, (b) **TiO_2/Fe-Por**, and (c) **TiO_2/Hem** after laser excitation at λ = 355 nm and application of an external bias. "hs" denotes scavenging of holes by TEOA as a hole scavenger. (1) and (4) denote light excitation of TiO_2 and iron porphyrins, (2) and (5) denote the back-electron-transfer processes between the TiO_2 (CB) to TiO_2 (VB) and Fe-Por* to Fe-Por, (3) denotes the charge/electron transfer from TiO_2 (CB) to an adsorbed CO_2 molecule, (3′) denotes the charge transfer from Fe-Por* to an adsorbed CO_2 molecule, and (6) and (7) represent the back-electron-transfer processes from the reduced Fe-Por* to TiO_2 (CB) and TiO_2 (CB) to the Fe-Por ground state or to the electrolyte. At the bottom, CO_2 reduction potentials are given for different product formations in aqueous and acetonitrile solvents.

commencement of the CO_2 reduction catalysis. In the oxidative scan, the peak observed at −1.5 V vs Ag/AgCl is ascribed to the oxidation of some Ti^{3+} to Ti^{4+} state (Figure S13b,c). The CVs of **TiO_2/Hem** and **TiO_2/Fe-Por** film electrodes under an argon atmosphere did not display the diagnostic redox couples for three iron-centered reversible reactions. In **TiO_2/Hem**, a reduced signal at −1.47 V and in the oxidative scan a peak at −1.40 V were noted (Figure S13a). For **TiO_2/Fe-Por** a reversible wave at −1.12 V vs Ag/AgCl was observed. However, in the presence of CO_2, both **TiO_2/Hem** and **TiO_2/Fe-Por** films showed a catalytic reduction current starting at an onset potential of ∼−1.3 V. The onset potential of the catalytic currents of the hybrid films is also similar to that of the bare **TiO_2** film (Figure S13b,c).

The electro-, photo-, and photoelectrochemical CO_2R product selectivities of the hybrid assemblies were further evaluated using controlled-potential electrolysis, at potentials ranging from −0.5 to −1.8 V vs Ag/AgCl of the CO_2-saturated acetonitrile solutions. The evolved gases were analyzed using gas chromatography, and no liquid products were detected in solution. CO and CH_4 were obtained as CO_2 reduction products and H_2 was also formed in some cases (Figures S14 and S15). The obtained results are summarized in Table 1. Under electrochemical conditions, the **TiO_2** film produced a small amount of CO only when the applied potential reached a value of −1.8 V vs Ag/AgCl, although under those conditions, H_2 was the main product (15% CO selectivity). In contrast, the simple irradiation of the **TiO_2** film with a 365 nm LED light produced the formation of CO and a trace of CH_4. The application of a bias potential of −0.5 V to the light-irradiated electrode did not modify the production of CO but initiated significant formation of CH_4 (∼50% selectivity). At −1.25 V, the production rates of the two gases increased, maintaining a similar product selectivity. However, at −1.5 V, H_2 evolved as the major product. CO was also produced (∼30% selectivity), but no CH_4 was detected. Taken together, these observations support that the photoelectrons injected in the conduction band of TiO_2 are responsible for the photoelectrochemically catalyzed CO_2R occurring at lower overpotentials (−0.5 to −1.5 V) than that required under pure electrochemical conditions (−1.8 V). Also, under light irradiation, it is possible to obtain CH_4, the 8-electron-reduction product of CO_2, along with suppression of the undesired HER. Previously, it was described that Ti^{3+} sites could enhance the chemisorption of CO_2 and entail its activation to undergo C−O bond cleavage.[46] Also, the photogenerated electrons accumulated in the TiO_2 intraband states were claimed to facilitate multielectron-transfer processes, generating C_2 and C_3 hydrocarbons.[47] Nevertheless, we have not observed the presence of C_2 and C_3 products in the present study.

Both **TiO_2/Hem** and **TiO_2/Fe-Por** hybrid films exclusively formed CO as the CO_2R product using either electro- or photoelectrochemical conditions. Under electrochemical conditions, the **TiO_2/Hem** film started to furnish CO starting at −1.5 V, but under light irradiation the **TiO_2/Hem** film started formation of CO starting at −0.5 V. However, at −0.5 and −1.25 V, the rate of formation of CO became similar to that of bare TiO_2 (Table 1). Formation of CO under light irradiation increased drastically at −1.5 V. For the **TiO_2/Fe-Por** film, only light irradiation furnishes CO formation similar to that observed in previous **TiO_2** and **TiO_2/Hem** cases. A slight increase in the CO formation catalyzed by the **TiO_2/Fe-Por** film was observed under the photoelectrochemical conditions at −0.5 V applied bias (Table 1). As indicated, the **TiO_2/Fe-Por** hybrid system was unstable in controlled-potential electrolysis at further potentials more negative than −0.8 V; thus, we were restricted to further explore its activity for the CO_2R.

It is worth noting that we did not detect the formation of CO_2R products under pure electrochemical conditions (without light irradiation) using the TiO_2-sensitized/hybrid films in the range of applied bias (0 to −1 V vs Ag/AgCl) used for the L-TAS measurements. The studied TiO_2 hybrid films show a reduced performance in the CO_2R reaction compared to

https://doi.org/10.1021/acsami.2c22458
ACS Appl. Mater. Interfaces 2023, 15, 14304−14315

reported analogous hybrid assemblies of FTO and FTO-SnO_2-supported Fe porphyrin dimer.[22] Nevertheless, it is remarkable that the TiO_2-sensitized films reported here (**TiO_2/Hem** and **TiO_2/Fe-Por**) can be used as highly selective (100% CO selectivity) photocathodes. Also, the superior performance of the materials for the formation of CO_2R products, under the photoelectrochemical conditions at much more positive reduction potentials, indicates that the photogenerated electrons within the sensitized TiO_2 hybrid films play a pivotal role in the catalysis.

3. DISCUSSION

In this work, we report our results of CO_2 reduction catalysis using nanocrystalline mesoporous **TiO_2** and **TiO_2**/iron porphyrin hybrid films. The reported findings are supported by the characterization of the decay dynamics of the photoinduced charge transfer processes occurring in the films using micro- to millisecond L-TAS spectroscopy. Previously, it was reported that the conduction band electrons of TiO_2 can be trapped in the intraband defect states of the surface and the bulk. The electron entrapment strongly influences the charge transport properties of the TiO_2 film.[48] In addition, the application of a negative potential results in the accumulation of electrons in the conduction and intraband trap states. The accumulation of the electrons produced a modulation of the Fermi level of the TiO_2 electrode. The rate of charge recombination increases as the applied negative voltage does.[49] In fact, we observed that in the range of 0−0.8 V (vs Ag/AgCl) applied voltage, the nanocrystalline mesoporous **TiO_2** displayed a maximum ΔOD transient absorption in comparison to an analogous experiment without any applied voltage bias (Figure 3a,d). This is due to the continuum filling of the electrons in the valence band to the Fermi level of the TiO_2 electrode. The $t_{50\%}$ value (0.0041 s) at −0.5 V applied bias is smaller than that measured without applying a bias voltage (0.012 s). This result demonstrated that the application of a bias voltage caused a significant increase in the rate of charge recombination (65% reduction in $t_{50\%}$ value) (Figure 4a). In Figure 5a, we denoted the charge recombination process (2), occurring in the millisecond to second time scale, as that observed in the transient absorption decay process of the **FTO-TiO_2** film. In the presence of CO_2 and under a −0.5 V bias, a decrease in both the transient absorption (∼35%) and $t_{50\%}$ values (50%) are noted (Figure 4a). This indicates that the photogenerated electrons at the TiO_2 surface are rapidly transferred (faster than 10 ms) to the adsorbed CO_2 molecule at the surface and further reduction (process (3) in Figure 5a and Figure 3a) to C_1 products. Also, the presence of the adsorbed CO_2 molecules causes (process (3)) faster charge recombination of the TiO_2 excited electrons. Subsequently, we tested our hypothesis by performing controlled-potential electrolysis using **FTO-TiO_2** films as electrodes under similar conditions employed for the TAS experiments. Our aim was to detect the formation of any multielectron-assisted CO_2R product triggered by the accumulated photogenerated TiO_2 electrons. Table 1 shows that the photogenerated TiO_2 electrons induced the formation of both CO ($2e^-$) and CH_4 ($8e^-$) products in either the presence or absence of a voltage bias. The use of the TiO_2 electrode under typical electrochemical conditions required an applied voltage of at least −1.8 V to induce the formation of products and furnish CO and H_2.

It worth noting that, based on the standard potential values for the reduction reactions of CO_2 to CO and CH_4 in H_2O and acetonitrile solution,[50−53] there is a gain in the overpotential value when the **FTO-TiO_2** electrode is used under photoelectrochemical conditions. This result correlates directly with the faster charge recombination kinetics measured in the corresponding TAS experiments. To the best of our knowledge, this is the first report studying the charge transfer kinetics of mesoporous **TiO_2** films during CO_2 reduction, monitoring the micro-/millisecond lifetimes of the photoexcited electrons of TiO_2. In the L-TAS measurement, TEOA was used in excess as a hole scavenger. However, TEOA can also bind at the TiO_2 surface, as well as induce the formation of a zwitterionic alkylcarbonate adduct[54] with CO_2 that also interacts with the surface via unreacted terminal −OH groups. The two surface binding processes involving TEOA may produce a faster decay in the L-TAS experiments, as observed for the TiO_2 electrodes. For our electrolysis studies, we did not use TEOA. Nevertheless, multiple reports have described the use of TEOA as a sacrificial electron donor for the catalytic CO_2 reduction in organic media.[54−56] The presence of TEOA can alter the reaction rate and the product selectivity of the CO_2 reduction, but it does not inhibit the reaction.

For the **TiO_2/Hem** and **TiO_2/Fe-Por** hybrid films the situation changed. In an ideal photocathode, electron transfer from the TiO_2 conduction band to the iron porphyrins is desired. This process should cause the reduction of the iron metal center and subsequent CO_2 activation/reaction. However, both TiO_2 and iron porphyrins absorb light in the visible region. The light absorption initiates intra- and interfacial electron communications within the **TiO_2/Iron** porphyrin hybrid systems. The standard potential of the TiO_2 conduction band (−0.85 V vs NHE) is well below the reduction potential of the $Fe^{II/I}$ and $Fe^{I/0}$ processes of iron porphyrins (**Hem**, −1.03, −1.61 V; **Fe-Por**, −0.86, −1.47 V vs NHE). Fe^I and Fe^0 are potent reductants to activate the reduction of CO_2. Considering that in the hybrids film the energy levels of the different redox states are similar to those in acetonitrile solution, the electron transfer from the photoexcited **Hem** and **Fe-Por** units to the conduction band of TiO_2 is feasible and thermodynamically favored.[57] In fact, the micro- to millisecond L-TAS spectra of **TiO_2/Hem** and **TiO_2/Fe-Por** imply the existence of such an interfacial charge transfer process. The excitation with 355 nm light initiates ultrafast electron injection in the excited state of the iron porphyrins from the ground singlet states, which can be recombined back (processes (4) and (5) in Figure 5b,c), producing a transient signal. However, the rate of this recombination step (5) for iron porphyrins is known to occur in the pico- to femtosecond time scale.[43,44,58−60] Consequently, it is not possible to detect this process in the presented data set due to the time resolution limitation of the used equipment. Two additional interfacial charge transfer processes can be foreseen: process (6), corresponding to the photoinjection of electrons in the TiO_2 conduction band/intraband states from the excited state of the iron porphyrins, and process (7) corresponding to the back electron transfer from the TiO_2 conduction band to the oxidized porphyrin ground state (Figure 5b,c). From the spectra shown in Figure 3b,c, it is evident that from 10 μs to 1 ms similar decay signals are observed for the both iron porphyrins, which are quite different from that measured for the reference **TiO_2** film, recorded at the same time. Thereby, considering Figure 5b,c, we suggest that the decay of the

https://doi.org/10.1021/acsami.2c22458
ACS Appl. Mater. Interfaces 2023, 15, 14304−14315

TiO_2/iron porphyrin film signals does not correspond to the recombination process (2). The decay of the signal is fast (decay in 1 ms) compared to that of electrons in the conduction band of **TiO_2** (up to 0.1 s) (Figures 3a and 5a). Comparing the electron transfer processes (6) and (7), it is more likely that process (6) (nano- to microsecond) exhibits faster relaxation dynamics than process (7) (micro- to millisecond). Hence, the transient signals in Figure 3b,c featuring decays in the 10 ms scale are attributed to the electron-transfer process (7). In this process, the oxidized iron porphyrin cation is being reduced by the back-electron transfer from electrons accumulated or photoinjected in the TiO_2 conduction band/intraband states. The relative position of the oxidized porphyrin cation makes process (7) energetically more favorable than process (2), leading to ∼100 times faster decay of the L-TAS signals in the hybrid materials. In the presence of CO_2, the photoexcited electrons can be transferred to the adsorbed CO_2 molecule on the surface. This is depicted via processes (3) (from the conduction band of TiO_2) and (3′) (from excited state of the iron porphyrin). Electron-transfer processes (4), (6), and (7) take place efficiently in a closed-loop manner within the covalently attached iron porphyrins and the TiO_2 interface. This is detrimental to the direct transfer of photogenerated electrons to adsorbed CO_2 molecules (processes (3) and (3′)). This hypothesis could serve to explain our observations related to not having significant changes in the decays of the transient absorption signals for **TiO_2/Hem** and **TiO_2/Fe-Por** hybrid films in the presence or absence of CO_2 (Figure 3b,c). The presence of TEOA as a hole scavenger has no effect on the stabilization of the oxidized iron porphyrin cation state (Figure 5b,c and Figure S9b,c). Therefore, and in agreement with experiment, the decay of the signals corresponding to process (7) are not modified. In support of these L-TAS observations, photoelectrocatalysis results confirm that both **TiO_2**/iron porphyrin systems form CO as the reduced product at −0.5 V with 100% selectivity. As shown in Table 1, under photoelectrocatalysis conditions with an applied voltage bias of −0.5 V, the rates of product formation for bare **TiO_2** and for **TiO_2**/iron porphyrin films are similar; however, the TiO_2 film also produces CH_4. We conclude that the presence of the Fe porphyrins causes a change in product selectivity in favor of CO formation. Applying a more negative potential bias (≥−1 V) favors the reduction of the iron center in the porphyrin layer, resulting in a better CO_2 reduction performance. As explained above, we do not observe any L-TAS signals in this range due to faster back-electron transfer between the electrons at the TiO_2 and the oxidized porphyrin catalysts.

4. CONCLUSION

In summary, we determined the charge transfer kinetics of mesoporous **TiO_2** and two **TiO_2**/iron porphyrin hybrid films by employing L-TAS. The results were corroborated by those obtained in the evaluation of their performance as photocathodes in the CO_2R. Our findings demonstrate that the kinetics and the nature of the photoinduced electron transfer, as well as charge recombination processes occurring in the films, have a noticeable impact on the efficient electron transfer to the adsorbed CO_2 molecules and their CO_2R reactivity. Under excitation with λ = 355 nm light and applied external bias, the photogenerated electrons in bare **TiO_2** showed a large decay of the transient signal intensity of the charge-separated state. In contrast, we observed faster recombination kinetics in the presence of CO_2 and TEOA, used as a hole scavenger. For the **TiO_2**/iron porphyrin films, the recombination kinetics of the charge-separated states were fast and not modified in the presence of CO_2. The efficiencies of the materials in the CO_2R were comparable. Although the film functionalized with Hemin units is quite stable, the analogue based on the iron porphyrin had leaching issues at moderate negative bias potentials.

The interfacial charge recombination processes, occurring between the oxidized iron porphyrin and the electrons in the conduction band of TiO_2, caused a diminution of the direct charge transfer process to the CO_2 molecules. This phenomenon is translated into a depletion of the CO_2 reduction efficiencies of the hybrid film materials. Under photo- and photoelectrochemical conditions, the **TiO_2** film produced CO and CH_4 as CO_2 reduction products at potentials ranging from 0 to −1.25 V. In contrast, **TiO_2/Hem** and **TiO_2/Fe-Por** films exclusively produced CO under comparable conditions. All films were better cathodes under light irradiation, in terms of efficiency and overpotential requirement for the CO_2R. This finding made us investigate in detail the electron-/charge-transfer processes occurring in the materials. We emphasize that the use of L-TAS we applied for the investigation of the photochemical CO_2 reduction could be extended to a wide variety of catalytic systems. Using this methodology, it is possible to gain further insight into the charge-transfer kinetics occurring at the catalyst surface. We anticipate that a better understanding of the detrimental steps involved in the interfacial charge-transfer processes and other limiting factors regarding the stability of the **TiO_2**/iron porphyrin assemblies will help significantly in designing improved and unprecedented metalloporphyrin-semiconductor-based photocathodes for the CO_2R.

5. EXPERIMENTAL SECTION

5.1. Materials and Reagents. All reagents, including pyrrole, pentylbenzene, methyl 4-formylbenzoate, acetic acid 99%, Hemin ≥96%, acetonitrile and *N*,*N*-dimethylformamide anhydrous 99.8% (ACN and DMF), triethanolamine 99% (TEOA), tetrabutylammonium hexafluorophosphate ≥99.0% ($TBAPF_6$), 2,6-lutidine, and iron(II) bromide ($FeBr_2$) were purchased from Sigma-Aldrich and were used as received without further purification. $TBAPF_6$ was dried under vacuum before use. FTO conducting glass substrates (TEC 15 Ω/cm^2 resistance) were purchased from Xop Glass, Castellón, Spain. Nanocrystalline titania paste was purchased from Dyesol (30NR-D titania paste, 20 nm particle size). Aluminum oxide, 20% in H_2O, colloidal dispersion was purchased from Alfa Aesar.

5.2. Alumina Paste Synthesis. The Al_2O_3 paste was prepared using a commercial water-based colloidal dispersion of Al_2O_3 nanoparticles with a uniform diameter of 50 nm (Alfa-Aesar). Briefly, 37.5 mg of Al_2O_3 solution and 3 mg of acetic acid 99% were mixed and stirred for 1.5 days, until the mixture became thick.

5.3. TiO_2 and Al_2O_3 Porphyrin Film Fabrication. A nanocrystalline TiO_2/Al_2O_3 paste was deposited onto FTO conducting glass substrate by the well-known doctor blade technique. The glass-FTO substrate was previously cleaned by washing with soap, distilled water, and ethanol and dried by heating at 500 °C for 15 min. After the film fabrication, the resulting films were dried for ∼30 min at room temperature and gradually heated in a muffle furnace at 325 °C for 5 min, 375 °C for 5 min, 450 °C for 15 min, and 500 °C for 15 min for sintering. The glass films, with a resulting thickness of 4−5 μm, were cut into pieces with an active area of 1 cm^2. TiO_2/Al_2O_3 electrodes were functionalized by dip-coating into a solution of 0.5 mM Hemin (**Hem**) or 0.5 mM Porphyrin (**Fe-Por**) in MeOH for 30 min at room temperature in the dark. Afterward, they were rinsed with MeOH, dried with air, and placed in an oven at 70 °C for 1 h.

https://doi.org/10.1021/acsami.2c22458
ACS Appl. Mater. Interfaces 2023, 15, 14304−14315

5.4. TiO_2 and Al_2O_3 Porphyrin Film Electrode Preparation. An electrical wire connection to the small glass film (electrode with 1 cm^2 area) was made by using ultrasonic shouldering (USS-9210, MBR electronics) systems and Cerasolzer as an active solder alloy. Except for the TiO_2-coated film area, other parts of the electrode were well-wrapped with Teflon tape before placing it inside the electrochemical/TAS measurement cell to protect it from any types of solvent-assisted contamination during the measurements.

5.5. Transient Spectroscopic Characterization Techniques. The charge-transfer dynamics of TiO_2/Al_2O_3 iron porphyrin films were measured using laser transient absorption spectroscopy (L-TAS) from the microseconds to milliseconds time scale at room temperature. Measurements were carried out employing a NdYAG laser as the excitation source (355 nm, 7 ns pulse width, 1 mJ of power) and a 150 W tungsten lamp as the light probe. All experiments were performed in a homemade Teflon cell with two quartz windows. The cell was purged with N_2 for 15 min filled with anhydrous $TBAPF_6$/acetonitrile (0.1 M) electrolyte, containing 0.01 M triethanolamine (TEOA) when stated. For measurements under CO_2, the electrolyte was purged with CO_2 for 15 min. Bias was applied using a Keithley 2400 instrument in a 4-wire configuration as a potentiostat. Ag/AgCl (1 M KCl) was used as the reference electrode, and Pt wire was used as the counter electrode.

5.6. Electrochemical and Photoelectrochemical Measurements. All the electrochemical experiments were carried out with a Bio-Logic potentiostat equipped with EC-Lab software in a homemade single-compartment glass cell. Ag/AgCl (1 M KCl) was used as the reference electrode, Pt wire was used as the counter electrode, and a **TiO_2** or **TiO_2**/iron porphyrin film was used as the working electrode. The cell was purged with Ar for 15 min, and it was filled with anhydrous acetonitrile/$TBAPF_6$ (0.1 M) electrolyte prior to the measurements. For measurements under CO_2, the electrolyte was purged with CO_2 for 15 min. For controlled-potential electrolysis (CPE), the same single-compartment glass cell was used. The cell was purged with CO_2 for 15 min and filled with anhydrous acetonitrile/$TBAPF_6$ (0.1 M) electrolyte, followed by purging for 15 min more. The counter electrode bridge was filled with 0.05 M Et_4COONH_4 salt along with acetonitrile/$TBAPF_6$ (0.1 M) electrolyte. Then, the CO_2 flow was removed, ensuring the perfect sealing of the cell. The electrolyte was maintained under constant stirring in the course of the experiment. During the photoelectrochemical experiments, a homemade single-compartment glass cell with a one-sided quartz window was used for the electrolysis experiment, keeping the same electrolyte and reference, counter, and working electrodes as mentioned for the electrochemical experiments. The electrode was irradiated with a high-power light source purchased from Sahlmann Photochemical Solutions consisting of 3 LED diodes from Nichia (365 nm, 241.5 mW cm^{-2}). The sample was located 1.5 cm from the power source (LED). The CO_2 reduction gaseous product was characterized with an Agilent GC instrument by manual injection of the sample taken from the head space of the glass cell by gastight Hamilton micro syringe. The GC is configured with HP-PLOT-Q and a Molesieve column, argon as the carrier gas, and flame ionization (CH_4, CO) and thermal conductivity (H_2) detectors (FID and TCD). The calibration of each gas (CH_4, CO, H_2) were done prior to the CPE measurements using a standard mixture of the analyte gases obtained from Messer. The product selectivity (SE) and turnover numbers (TON) were calculated following a standard literature practice.[61,62]

■ ASSOCIATED CONTENT

Supporting Information

The Supporting Information is available free of charge at https://pubs.acs.org/doi/10.1021/acsami.2c22458.

Synthesis of **Fe-Por**, UV−vis spectra of **Fe-Por**, ^1H NMR spectra of **Fe-Por**, MALDI mass of **Fe-Por**, adsorption kinetics of **Hem** and **Fe-por** on TiO_2, IR spectra of **FTO-TiO_2/Fe-Por** and **FTO-TiO_2/Hem**, XPS of **FTO-TiO_2**, **FTO-TiO_2/Fe-Por**, and **FTO-TiO_2/Hem**, TAS of **TiO_2**, **TiO_2/Fe-Por**, and **TiO_2/Hem** under bias, no external bias, and different conditions, CV of **Hem** and **Fe-Por** in DMF, CV of **TiO_2**, **TiO_2/Hem**, and **TiO_2/Fe-Por** films in DMF, GC chromatogram for the CO and CH_4 gases measured after an electrolysis study (PDF)

■ AUTHOR INFORMATION

Corresponding Authors

Tamal Chatterjee − *Institute of Chemical Research of Catalonia (ICIQ), The Barcelona Institute of Science and Technology, 43007 Tarragona, Spain*; Email: tchatterjee@iciq.es

Pablo Ballester − *Institute of Chemical Research of Catalonia (ICIQ), The Barcelona Institute of Science and Technology, 43007 Tarragona, Spain; Catalan Institution for Research and Advanced Studies (ICREA), 08018 Barcelona, Spain;* orcid.org/0000-0001-8377-6610; Email: pballester@iciq.es

Emilio Palomares − *Institute of Chemical Research of Catalonia (ICIQ), The Barcelona Institute of Science and Technology, 43007 Tarragona, Spain; Catalan Institution for Research and Advanced Studies (ICREA), 08018 Barcelona, Spain;* orcid.org/0000-0002-5092-9227; Email: epalomares@iciq.es

Authors

Beatriu Domingo-Tafalla − *Institute of Chemical Research of Catalonia (ICIQ), The Barcelona Institute of Science and Technology, 43007 Tarragona, Spain; Universitat Rovira i Virgili (URV), Departament D'enginyeria electrònica Elèctrica i Automàtica, Avinguda Països Catalans, 43007 Tarragona, Spain;* orcid.org/0000-0001-8579-7677

Federico Franco − *Institute of Chemical Research of Catalonia (ICIQ), The Barcelona Institute of Science and Technology, 43007 Tarragona, Spain*

Javier Perez Hernandez − *Institute of Chemical Research of Catalonia (ICIQ), The Barcelona Institute of Science and Technology, 43007 Tarragona, Spain;* orcid.org/0000-0002-8503-5717

Eugenia Martinez-Ferrero − *Institute of Chemical Research of Catalonia (ICIQ), The Barcelona Institute of Science and Technology, 43007 Tarragona, Spain;* orcid.org/0000-0001-7558-0271

Complete contact information is available at: https://pubs.acs.org/10.1021/acsami.2c22458

Notes

The authors declare no competing financial interest.

■ ACKNOWLEDGMENTS

B.D.-T. is thankful to the MCIN and ESF for a predoctoral grant (PRE2020-092525). T.C. thanks the NEFERTITI (H2020) project for a postdoctoral fellowship (Grant agreement ID: 101022202). F.F. thanks MCIN/AEI/10.13039/501100011033 for a Juan de la Cierva-Incorporación fellowship (IJC2019-042363-I). Funding from MINECO (project PID2019-109389RB-I00) and SGR-AGAUR (project 2021SGR01261) is also acknowledged. E.P. gratefully acknowledges financial support from ICIQ, MINECO, and ICREA.

REFERENCES

(1) Nocera, D. G. Solar Fuels and Solar Chemicals Industry. *Acc. Chem. Res.* **2017**, *50* (3), 616−619.

(2) Segev, G.; Kibsgaard, J.; Hahn, C.; Xu, Z. J.; Cheng, W.-H. S.; Deutsch, T. G.; Xiang, C.; Zhang, J. Z.; Hammarström, L.; Nocera, D. G.; Weber, A. Z.; Agbo, P.; Hisatomi, T.; Osterloh, F. E.; Domen, K.; Abdi, F. F.; Haussener, S.; Miller, D. J.; Ardo, S.; McIntyre, P. C.; Hannappel, T.; Hu, S.; Atwater, H.; Gregoire, J. M.; Ertem, M. Z.; Sharp, I. D.; Choi, K.-S.; Lee, J. S.; Ishitani, O.; Ager, J. W.; Prabhakar, R. R.; Bell, A. T.; Boettcher, S. W.; Vincent, K.; Takanabe, K.; Artero, V.; Napier, R.; Cuenya, B. R.; Koper, M. T. M.; Van De Krol, R.; Houle, F. The 2022 Solar Fuels Roadmap. *J. Phys. D. Appl. Phys.* **2022**, *55* (32), 323003.

(3) Jiang, C.; Moniz, S. J. A.; Wang, A.; Zhang, T.; Tang, J. Photoelectrochemical Devices for Solar Water Splitting−Materials and Challenges. *Chem. Soc. Rev.* **2017**, *46* (15), 4645−4660.

(4) Tao, X.; Zhao, Y.; Wang, S.; Li, C.; Li, R. Recent Advances and Perspectives for Solar-Driven Water Splitting Using Particulate Photocatalysts. *Chem. Soc. Rev.* **2022**, *51* (9), 3561−3608.

(5) Stephens, I. E. L.; Chan, K.; Bagger, A.; Boettcher, S. W.; Bonin, J.; Boutin, E.; Buckley, A. K.; Buonsanti, R.; Cave, E. R.; Chang, X. 2022 Roadmap on Low Temperature Electrochemical CO_2 Reduction. *J. Phys. Energy* **2022**, *4* (4), 042003.

(6) Liu, C.; Colón, B. C.; Ziesack, M.; Silver, P. A.; Nocera, D. G. Water Splitting−Biosynthetic System with CO_2 Reduction Efficiencies Exceeding Photosynthesis. *Science (80-.).* **2016**, *352* (6290), 1210−1213.

(7) Karkas, M. D.; Verho, O.; Johnston, E. V.; Åkermark, B. Artificial Photosynthesis: Molecular Systems for Catalytic Water Oxidation. *Chem. Rev.* **2014**, *114* (24), 11863−12001.

(8) Garcia Osorio, D. A.; Neri, G.; Cowan, A. J. Hybrid Photocathodes for Carbon Dioxide Reduction: Interfaces for Charge Separation and Selective Catalysis. *ChemPhotoChem.* **2021**, *5* (7), 595−610.

(9) Kumagai, H.; Tamaki, Y.; Ishitani, O. Photocatalytic Systems for CO_2 Reduction: Metal-Complex Photocatalysts and Their Hybrids with Photofunctional Solid Materials. *Acc. Chem. Res.* **2022**, *55* (7), 978−990.

(10) Morikawa, T.; Sato, S.; Sekizawa, K.; Suzuki, T. M.; Arai, T. Solar-Driven CO_2 Reduction Using a Semiconductor/Molecule Hybrid Photosystem: From Photocatalysts to a Monolithic Artificial Leaf. *Acc. Chem. Res.* **2022**, *55* (7), 933−943.

(11) Kumar, S.; Ojha, K.; Ganguli, A. K. Interfacial Charge Transfer in Photoelectrochemical Processes. *Adv. Mater. Interfaces* **2017**, *4* (7), 1600981.

(12) Cohen, K. Y.; Evans, R.; Dulovic, S.; Bocarsly, A. B. Using Light and Electrons to Bend Carbon Dioxide: Developing and Understanding Catalysts for CO_2 Conversion to Fuels and Feedstocks. *Acc. Chem. Res.* **2022**, *55* (7), 944−954.

(13) Reynal, A.; Lakadamyali, F.; Gross, M. A.; Reisner, E.; Durrant, J. R. Parameters Affecting Electron Transfer Dynamics from Semiconductors to Molecular Catalysts for the Photochemical Reduction of Protons. *Energy Environ. Sci.* **2013**, *6* (11), 3291−3300.

(14) Bozal-Ginesta, C.; Mesa, C. A.; Eisenschmidt, A.; Francàs, L.; Shankar, R. B.; Antón-García, D.; Warnan, J.; Willkomm, J.; Reynal, A.; Reisner, E.; et al. Charge Accumulation Kinetics in Multi-Redox Molecular Catalysts Immobilised on TiO $_2$. *Chem. Sci.* **2021**, *12* (3), 946−959.

(15) Reynal, A.; Willkomm, J.; Muresan, N. M.; Lakadamyali, F.; Planells, M.; Reisner, E.; Durrant, J. R. Distance Dependent Charge Separation and Recombination in Semiconductor/Molecular Catalyst Systems for Water Splitting. *Chem. Commun.* **2014**, *50* (84), 12768−12771.

(16) Clifford, J. N.; Martínez-Ferrero, E.; Viterisi, A.; Palomares, E. Sensitizer Molecular Structure-Device Efficiency Relationship in Dye Sensitized Solar Cells. *Chem. Soc. Rev.* **2011**, *40* (3), 1635−1646.

(17) Dong, Y.; Nie, R.; Wang, J.; Yu, X.; Tu, P.; Chen, J.; Jing, H. Photoelectrocatalytic CO2 Reduction Based on Metalloporphyrin-Modified TiO_2 Photocathode. *Chin. J. Catal.* **2019**, *40* (8), 1222−1230.

(18) Mendieta-Reyes, N. E.; Cheuquepán, W.; Rodes, A.; Gómez, R. Spectroelectrochemical Study of CO_2 Reduction on TiO_2 Electrodes in Acetonitrile. *ACS Catal.* **2020**, *10* (1), 103−113.

(19) Nguyen, T. P.; Nguyen, D. L. T.; Nguyen, V.-H.; Le, T.-H.; Vo, D.-V. N.; Trinh, Q. T.; Bae, S.-R.; Chae, S. Y.; Kim, S. Y.; Le, Q. V. Recent Advances in TiO_2-Based Photocatalysts for Reduction of CO_2 to Fuels. *Nanomaterials* **2020**, *10* (2), 337.

(20) Gotico, P.; Halime, Z.; Aukauloo, A. Recent Advances in Metalloporphyrin-Based Catalyst Design towards Carbon Dioxide Reduction: From Bio-Inspired Second Coordination Sphere Modifications to Hierarchical Architectures. *Dalt. Trans.* **2020**, *49* (8), 2381−2396.

(21) Boutin, E.; Merakeb, L.; Ma, B.; Boudy, B.; Wang, M.; Bonin, J.; Anxolabéhère-Mallart, E.; Robert, M. Molecular Catalysis of CO_2 Reduction: Recent Advances and Perspectives in Electrochemical and Light-Driven Processes with Selected Fe, Ni and Co Aza Macrocyclic and Polypyridine Complexes. *Chem. Soc. Rev.* **2020**, *49* (16), 5772−5809.

(22) Mohamed, E. A.; Zahran, Z. N.; Naruta, Y. Efficient Heterogeneous CO_2 to CO Conversion with a Phosphonic Acid Fabricated Cofacial Iron Porphyrin Dimer. *Chem. Mater.* **2017**, *29* (17), 7140−7150.

(23) Khusnutdinova, D.; Beiler, A. M.; Wadsworth, B. L.; Jacob, S. I.; Moore, G. F. Metalloporphyrin-Modified Semiconductors for Solar Fuel Production. *Chem. Sci.* **2017**, *8* (1), 253−259.

(24) Pugliese, E.; Gotico, P.; Wehrung, I.; Boitrel, B.; Quaranta, A.; Ha-Thi, M.-H.; Pino, T.; Sircoglou, M.; Leibl, W.; Halime, Z.; Aukauloo, A. Dissection of Light-Induced Charge Accumulation at a Highly Active Iron Porphyrin: Insights in the Photocatalytic CO_2 Reduction. *Angew. Chemie Int. Ed.* **2022**, *61* (14), e202117530.

(25) Costentin, C.; Saveant, J.-M. Towards an Intelligent Design of Molecular Electrocatalysts. *Nat. Rev. Chem.* **2017**, *1* (11), 0087.

(26) Ardo, S.; Achey, D.; Morris, A. J.; Abrahamsson, M.; Meyer, G. J. Non-Nernstian Two-Electron Transfer Photocatalysis at Metalloporphyrin−TiO_2 Interfaces. *J. Am. Chem. Soc.* **2011**, *133* (41), 16572−16580.

(27) Forneli, A.; Planells, M.; Sarmentero, M. A.; Martinez-Ferrero, E.; O'Regan, B. C.; Ballester, P.; Palomares, E. The Role of Para-Alkyl Substituents on Meso-Phenyl Porphyrin Sensitised TiO_2 Solar Cells: Control of the e TiO_2/Electrolyte$^+$ Recombination Reaction. *J. Mater. Chem.* **2008**, *18* (14), 1652−1658.

(28) Walker, F. A.; Simonis, U. Iron Porphyrin Chemistry. *Encycl. Inorg. Chem.* **2006**, *2*, 2390−2521.

(29) Koenig, J. D. B.; Willkomm, J.; Roesler, R.; Piers, W. E.; Welch, G. C. Electrocatalytic CO_2 Reduction at Lower Overpotentials Using Iron (III) Tetra (Meso-Thienyl) Porphyrins. *ACS Appl. Energy Mater.* **2019**, *2* (6), 4022−4026.

(30) Azcarate, I.; Costentin, C.; Robert, M.; Savéant, J.-M. Through-Space Charge Interaction Substituent Effects in Molecular Catalysis Leading to the Design of the Most Efficient Catalyst of CO_2-to-CO Electrochemical Conversion. *J. Am. Chem. Soc.* **2016**, *138* (51), 16639−16644.

(31) Qu, Q.; Geng, H.; Peng, R.; Cui, Q.; Gu, X.; Li, F.; Wang, M. Chemically Binding Carboxylic Acids onto TiO_2 Nanoparticles with Adjustable Coverage by Solvothermal Strategy. *Langmuir* **2010**, *26* (12), 9539−9546.

(32) Al-Attafi, K.; Nattestad, A.; Yamauchi, Y.; Dou, S. X.; Kim, J. H. Aggregated Mesoporous Nanoparticles for High Surface Area Light Scattering Layer TiO_2 Photoanodes in Dye-Sensitized Solar Cells. *Sci. Rep.* **2017**, *7* (1), 10341.

(33) Yu, I. G.; Kim, Y. J.; Kim, H. J.; Lee, C.; Lee, W. I. Size-Dependent Light-Scattering Effects of Nanoporous TiO_2 Spheres in Dye-Sensitized Solar Cells. *J. Mater. Chem.* **2011**, *21* (2), 532−538.

(34) Sun, Z.-C.; She, Y.-B.; Zhou, Y.; Song, X.-F.; Li, K. Synthesis, Characterization and Spectral Properties of Substituted Tetraphenylporphyrin Iron Chloride Complexes. *Molecules* **2011**, *16* (4), 2960−2970.

https://doi.org/10.1021/acsami.2c22458
ACS Appl. Mater. Interfaces 2023, 15, 14304−14315

(35) Roales, J.; Pedrosa, J. M.; Guillén, M. G.; Lopes-Costa, T.; Castillero, P.; Barranco, A.; González-Elipe, A. R. Free-Base Carboxyphenyl Porphyrin Films Using a TiO_2 Columnar Matrix: Characterization and Application as NO_2. *Sensors. Sensors* **2015**, *15* (5), 11118−11132.
(36) Ding, Z.; Lu, G. Q.; Greenfield, P. F. Role of the Crystallite Phase of TiO_2 in Heterogeneous Photocatalysis for Phenol Oxidation in Water. *J. Phys. Chem. B* **2000**, *104* (19), 4815−4820.
(37) Patrocínio, A. O. T.; Paniago, E. B.; Paniago, R. M.; Iha, N. Y. M. XPS Characterization of Sensitized N-TiO_2 Thin Films for Dye-Sensitized Solar Cell Applications. *Appl. Surf. Sci.* **2008**, *254* (6), 1874−1879.
(38) Zhong, Y.-Q.; Hossain, M. S.; Chen, Y.; Fan, Q.-H.; Zhan, S.-Z.; Liu, H.-Y. A Comparative Study of Electrocatalytic Hydrogen Evolution by Iron Complexes of Corrole and Porphyrin from Acetic Acid and Water. *Transit. Met. Chem.* **2019**, *44*, 399−406.
(39) Wang, X.; Kafizas, A.; Li, X.; Moniz, S. J. A.; Reardon, P. J. T.; Tang, J.; Parkin, I. P.; Durrant, J. R. Transient Absorption Spectroscopy of Anatase and Rutile: The Impact of Morphology and Phase on Photocatalytic Activity. *J. Phys. Chem. C* **2015**, *119* (19), 10439−10447.
(40) Tang, J.; Durrant, J. R.; Klug, D. R. Mechanism of Photocatalytic Water Splitting in TiO_2. Reaction of Water with Photoholes, Importance of Charge Carrier Dynamics, and Evidence for Four-Hole Chemistry. *J. Am. Chem. Soc.* **2008**, *130* (42), 13885−13891.
(41) Tamaki, Y.; Furube, A.; Murai, M.; Hara, K.; Katoh, R.; Tachiya, M. Dynamics of Efficient Electron−Hole Separation in TiO_2 Nanoparticles Revealed by Femtosecond Transient Absorption Spectroscopy under the Weak-Excitation Condition. *Phys. Chem. Chem. Phys.* **2007**, *9* (12), 1453−1460.
(42) Murai, M.; Tamaki, Y.; Furube, A.; Hara, K.; Katoh, R. Reaction of Holes in Nanocrystalline TiO_2 Films Evaluated by Highly Sensitive Transient Absorption Spectroscopy. *Catal. today* **2007**, *120* (2), 214−219.
(43) Rury, A. S.; Sension, R. J. Broadband Ultrafast Transient Absorption of Iron (III) Tetraphenylporphyrin Chloride in the Condensed Phase. *Chem. Phys.* **2013**, *422*, 220−228.
(44) Kar, P.; Sardar, S.; Alarousu, E.; Sun, J.; Seddigi, Z. S.; Ahmed, S. A.; Danish, E. Y.; Mohammed, O. F.; Pal, S. K. Impact of Metal Ions in Porphyrin-Based Applied Materials for Visible-Light Photocatalysis: Key Information from Ultrafast Electronic Spectroscopy. *Chem. - Eur. J.* **2014**, *20* (33), 10475−10483.
(45) Zhang, W.; Chen, Y. Experimental Determination of Conduction and Valence Bands of Semiconductor Nanoparticles Using Kelvin Probe Force Microscopy. *J. nanoparticle Res.* **2013**, *15*, 1−7.
(46) Pipornpong, W.; Wanbayor, R.; Ruangpornvisuti, V. Adsorption CO_2 on the Perfect and Oxygen Vacancy Defect Surfaces of Anatase TiO_2 and Its Photocatalytic Mechanism of Conversion to CO. *Appl. Surf. Sci.* **2011**, *257* (24), 10322−10328.
(47) Bai, Y.; Li, M.; Liu, X.; Han, J.; Zhu, X.; Ge, Q.; Wang, H. Ti3+ Defective TiO2/CdS Z-Scheme Photocatalyst for Enhancing Photocatalytic CO_2 Reduction to C1−C3 Products. *Ind. Eng. Chem. Res.* **2022**, *61* (25), 8724−8737.
(48) Schwarzburg, K.; Willig, F. Influence of Trap Filling on Photocurrent Transients in Polycrystalline TiO_2. *Appl. Phys. Lett.* **1991**, *58* (22), 2520−2522.
(49) Haque, S. A.; Tachibana, Y.; Klug, D. R.; Durrant, J. R. Charge Recombination Kinetics in Dye-Sensitized Nanocrystalline Titanium Dioxide Films under Externally Applied Bias. *J. Phys. Chem. B* **1998**, *102* (10), 1745−1749.
(50) Benson, E. E.; Kubiak, C. P.; Sathrum, A. J.; Smieja, J. M. Electrocatalytic and Homogeneous Approaches to Conversion of CO_2 to Liquid Fuels. *Chem. Soc. Rev.* **2009**, *38* (1), 89−99.
(51) Kumar, B.; Llorente, M.; Froehlich, J.; Dang, T.; Sathrum, A.; Kubiak, C. P. Photochemical and Photoelectrochemical Reduction of CO_2. *Annu. Rev. Phys. Chem.* **2012**, *63*, 541−569.
(52) Apaydin, D. H.; Tordin, E.; Portenkirchner, E.; Aufischer, G.; Schlager, S.; Weichselbaumer, M.; Oppelt, K.; Sariciftci, N. S. Photoelectrochemical Reduction of CO_2 Using Third-Generation Conjugated Polymers. *ChemistrySelect* **2016**, *1* (6), 1156−1162.
(53) Pegis, M. L.; Roberts, J. A. S.; Wasylenko, D. J.; Mader, E. A.; Appel, A. M.; Mayer, J. M. Standard Reduction Potentials for Oxygen and Carbon Dioxide Couples in Acetonitrile and N, N-Dimethylformamide. *Inorg. Chem.* **2015**, *54* (24), 11883−11888.
(54) Sampaio, R. N.; Grills, D. C.; Polyansky, D. E.; Szalda, D. J.; Fujita, E. Unexpected Roles of Triethanolamine in the Photochemical Reduction of CO_2 to Formate by Ruthenium Complexes. *J. Am. Chem. Soc.* **2020**, *142* (5), 2413−2428.
(55) Pellegrin, Y.; Odobel, F. Sacrificial Electron Donor Reagents for Solar Fuel Production. *Comptes Rendus Chim.* **2017**, *20* (3), 283−295.
(56) Sahara, G.; Ishitani, O. Efficient Photocatalysts for CO_2 Reduction. *Inorg. Chem.* **2015**, *54* (11), 5096−5104.
(57) Liao, M.-S.; Scheiner, S. Electronic Structure and Bonding in Metal Porphyrins, Metal= Fe, Co, Ni, Cu, Zn. *J. Chem. Phys.* **2002**, *117* (1), 205−219.
(58) Obare, S. O.; Ito, T.; Meyer, G. J. Multi-Electron Transfer from Heme-Functionalized Nanocrystalline TiO_2 to Organohalide Pollutants. *J. Am. Chem. Soc.* **2006**, *128* (3), 712−713.
(59) Goncalves, P. J.; Sciuti, L. F.; Neto, N. M. B.; e Silva, R. C.; Silveira-Alves Jr, E.; Mendonça, C. R.; Zílio, S. C.; Borissevitch, I. E.; De Boni, L. Effects of PH on the Ultrafast Transient Absorption of Iron (III) Meso-Tetrakis (4-N-Methyl-Pyridiniumyl) Porphyrin (Fe3+ TMPyP) Molecular Complexes. *J. Photochem. Photobiol. A Chem.* **2021**, *408*, 113082.
(60) Lian, S.; Kodaimati, M. S.; Dolzhnikov, D. S.; Calzada, R.; Weiss, E. A. Powering a CO_2 Reduction Catalyst with Visible Light through Multiple Sub-Picosecond Electron Transfers from a Quantum Dot. *J. Am. Chem. Soc.* **2017**, *139* (26), 8931−8938.
(61) Kim, K.; Wagner, P.; Wagner, K.; Mozer, A. J. Electrochemical CO_2 Reduction Catalyzed by Copper Molecular Complexes: The Influence of Ligand Structure. *Energy Fuels* **2022**, *36* (9), 4653−4676.
(62) Windle, C. D.; Pastor, E.; Reynal, A.; Whitwood, A. C.; Vaynzof, Y.; Durrant, J. R.; Perutz, R. N.; Reisner, E. Improving the Photocatalytic Reduction of CO_2 to CO through Immobilisation of a Molecular Re Catalyst on TiO_2. *Chem. - Eur. J.* **2015**, *21* (9), 3746−3754.

https://doi.org/10.1021/acsami.2c22458
ACS Appl. Mater. Interfaces 2023, 15, 14304−14315